



On the origin of upper crustal shear-wave anisotropy at Samos Island, Greece

G. Kaviris¹ · I. Spingos¹ · V. Kapetanidis¹ · P. Papadimitriou¹ · N. Voulgaris¹

Received: 18 January 2021 / Accepted: 19 April 2021 / Published online: 11 May 2021 / Published online: 11 May 2021
© Institute of Geophysics, Polish Academy of Sciences & Polish Academy of Sciences 2021, corrected publication 2021

Abstract

Shear-wave splitting is associated to different sources in the upper crust. Preferentially oriented minerals, stress-aligned microcracks and tectonic structures have all been identified as causes of seismic anisotropy in the upper crust. However, distinguishing between them and discovering the actual origin of the splitting effect has important implications; changes in the anisotropic properties of the medium related to the behavior of fluid-filled microcracks could have potential connections to the occurrence of an impending significant earthquake. The recent 2020 Samos $M_w = 6.9$ event and its associated sequence was a great opportunity to study shear-wave splitting in the area. The spatial constrains in such studies, i.e., the requirement of events located very close to the receivers, did not permit exploring local anisotropy in the past, due to a severe lack of suitable data. To establish a background of splitting, we searched for any appropriate earthquake in a five-year period preceding the mainshock. We performed an automatic analysis on over 200 event-station pairs and obtained 164 high-quality splitting observations between January 2015 and November 2020. Results indicated a strong connection to local structures; S_{fast} polarization axes seem to align with faults in the area. However, we also observed a period of increasing and decreasing time-delays, associated with an $M_w = 6.3$ earthquake that occurred on June 2017 near Lesvos Island. The latter behavior implies the possibility of stress-induced anisotropy in the area. Thus, the Samos Island could be represented by two different sources of splitting; structures to the NW and microcracks to the SE.

Keywords Shear-wave splitting · Upper crust · Samos · Seismic anisotropy

Introduction

Seismic anisotropy is a well-known property of propagation media in the Earth, observed in multiple scales; from the mantle (Montagner and Tanimoto 1991; Salimbeni et al. 2008) to the crust (Boness and Zoback 2006a; Crampin et al. 1980; Crampin and Peacock 2005). It refers to changes in seismic velocity in respect to varying directions. In the case of Shear-wave Splitting (SwS), secondary S waves are polarized orthogonally when entering an anisotropic medium. This leads to the distinction of two waves. One travels with

the higher velocity (S_{fast}) and the other has a lesser velocity (S_{slow}). The S_{fast} is polarized in line with the dominant anisotropic feature of the medium, orienting its polarization direction (φ) accordingly. A measure of the strength of anisotropy is the time-delay (t_d) between the arrivals of the two shear-waves at the station. Oftentimes, to reduce the effect of the ray path, this quantity is normalized according to the source-receiver distance (t_n). Removing the effect of anisotropy can yield the polarization direction of the non-split shear-wave (p), as if the propagation medium were isotropic.

There is a variety of features that could act as the source of anisotropy. Mainly, a characteristic of the rock volume that the shear-waves traverse must be strongly oriented and homogeneously distributed. The lattice preferred orientation of minerals, either olivine for the upper mantle (Ismail and Mainprice 1998) or mica and other phyllosilicates in sedimentary and metamorphic lithologies for the crust (Paulssen 2004; Valcke et al. 2006), is commonly considered. There is a plethora of reports of mantle flow-related olivine layers affecting φ and causing splitting in teleseismic waves

Communicated by the Guest Editors: Ramon Zuñiga, Eleftheria Papadimitriou, Vassilios Karakostas and Onur Tan.

✉ G. Kaviris
gkaviris@geol.uoa.gr

¹ Department of Geology & Geoenvironment, Section of Geophysics-Geothermics, National and Kapodistrian University of Athens, Athens, Greece

(Evangelidis, 2017; Kaviris et al. 2018a; Kreemer, 2009). At a local scale, shear-wave splitting is frequently interpreted as induced by aligned microcracks which permeate the upper crust and fluids contained in them. Specifically, the Anisotropic Poro-Elasticity model (APE) provides a connection between regional stress and fluid processes, such as diffusion and migration (Crampin and Zatsepin 1997; Zatsepin and Crampin 1997). APE in tectonic regimes predicts a S_{fast} polarization axis oriented according to the maximum horizontal stress (S_{Hmax}). Moreover, APE has significant implications for earthquake forecasting. Since t_d works as a proxy for changes in the stress balance of a given rock volume, it can be used to extrapolate accumulation and release of stress associated with an impending strong seismic event (Gao and Crampin 2008). Such connections have been reported in literature (Crampin et al. 1999; Gao et al. 1998; Kaviris et al. 2018b), even though there are also cases debating this claim (Aster et al. 1990; Peng and Ben-Zion 2004). In any case, such variations have been better constrained in volcanic environments, preceding eruptions (Bianco and Zaccarelli 2008; Liu et al. 2010). There have also been observations of changes in the polarization of surface waves obtained from ambient noise, caused by crack-induced anisotropy, before an earthquake (Durand et al. 2011). Finally, shear-wave splitting has been attributed to the existence of dominant tectonic structures, such as faults, which dictate the S_{fast} polarization direction (Boness and Zoback 2006b; Zinke and Zoback 2000). According to the above, we can identify two possible origins of shear-wave splitting in the upper crust; (a) microcracks controlled by regional stress (stress-induced) and (b) tectonic structures (structurally-controlled).

There have been several shear-wave splitting studies in Greece. Polarization directions in the Western Gulf of Corinth (WGoC), where there is a rich archive of data, are usually oriented according to the S_{Hmax} , with a few exceptions that alignment to local faults is present (Bernard et al. 1997; Bouin et al. 1996; Giannopoulos et al. 2015; Kaviris et al. 2017, 2018b). Equivalently, splitting results in the Eastern Gulf of Corinth (Papadimitriou et al. 1999) and Eastern Attica seem to also agree with the APE model; there is even some indication of time-delay variations associated with a $M_w = 4.2$ event (Kaviris et al. 2018c). The Florina basin featured a more complex state of anisotropy, with a variety of polarization directions observed. However, this was probably affected by the local emission of CO_2 and its related processes (Kaviris et al. 2020). All three above-mentioned areas are characterized by normal faulting, as in the case of the earthquakes observed at Samos.

Samos is a Greek island located at the eastern Aegean Sea, about 2 km off the opposite coast of Turkey. The broader region's tectonics is mainly constituted by the SW motion of the Anatolia block, with a rate of about 30 mm/yr relative to a stable Eurasia (McClusky et al. 2000), mostly

accommodated along the North Anatolian Fault, a dextral strike-slip major structure (Papadimitriou and Sykes 2001), while the Hellenic subduction in the south is responsible for the extensional deformation of the Aegean microplate due to the subducting slab's rollback (Brun et al. 2016). In the vicinity of the Samos Island, the geodetic strain-rate field has a second invariant of 20–30 nstrain/yr (Kreemer 2009), mostly exhibiting elongation in a N-S to SSW-NNE direction, but also including a minor E-W shortening component and counter-clockwise rotation (Floyd et al. 2010). The stress-field that is derived from the inversion of focal mechanisms of crustal earthquakes indicates that the north Aegean is characterized by uniaxial extension in a SSW-NNE direction, while the maximum horizontal stress (S_{Hmax}) is mainly directed WNW-ESE (Kapetanidis and Kassaras 2019).

Given their geometry and kinematics (Fig. 1), the mapped active faults on Samos Island are capable of generating earthquakes with moment magnitude of the order of 6.3–6.8 (Chatzipetros et al. 2013). Historically, the broader region has been struck by strong earthquakes. In particular, several significant events of estimated $M_w > 5$ have reportedly occurred at the eastern part of the island in the eighteenth and nineteenth century (Fig. 1), with the more notable ones being the $M_w = 6.7$ event of 1751/06/18, the $M_w = 6.2$ event of 1873/02/01 and the $M_w = 6.2$ event of 1877/10/13 (Kouskouna and Sakkas 2013; Stucchi et al. 2013). Strong earthquakes near Samos Island have also been reported around 201–197 BC and 46–47 AD (Ambraseys 2015). During the instrumental era, the more recent significant earthquakes have been the $M_w = 6.0$ event of 1904/08/11, at the south-eastern part of the island, and the $M_w = 6.7$ event of 1955/07/16 near the Turkish coast ESE of the Samos Island (Makropoulos et al. 2012).

On 2020/10/30 11:51:28 UTC, a $M_w = 6.9$ earthquake occurred approximately 10 km offshore Samos Island (Ganas et al. 2020; Papadimitriou et al. 2020), generating the largest tsunami in the Aegean Sea since 1956 (Triantafyllou et al. 2021). The earthquake produced an aftershock sequence that extends 60 km in an E-W direction, including several events of moderate magnitude, the largest of which has been a $M_w = 5.0$ event, hours after the mainshock (Papadimitriou et al. 2020). The sequence was recorded by permanent seismological and accelerometric stations of the regional Hellenic Unified Seismological Network (HUSN; Evangelidis et al. 2021) in Greece, along with stations of the Boğaziçi University Kandilli Observatory and Earthquake Research Institute—Regional Earthquake-Tsunami Monitoring Center's (KOERI-RETMC) network in Turkey. To monitor the sequence, the Geodynamic Institute of the National Observatory of Athens (GI-NOA) installed two additional temporary stations on the island (SAM1 and SAM2; Fig. 1). In this study we take advantage of the recent sequence to

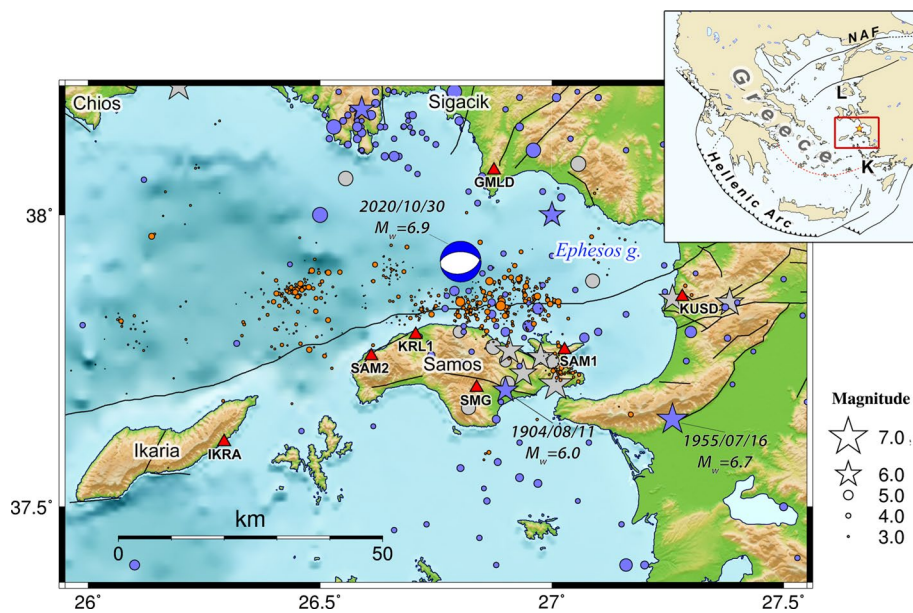


Fig. 1 Seismotectonic map of the broader Samos area. Seismicity (circles and stars, with size proportional to magnitude) are from SHEEC (years 1000–1899, gray; Stucchi et al. 2013), from the compilation of the Seismotectonic Atlas of Greece (1900–June 2020, $M \geq 4$, blue; Kassaras et al. 2020) and from a combined catalogue of routine analysis of seismicity at SL-NKUA and GI-NOA for the 2020 Samos aftershock sequence (2020/10/30–2020/11/30, orange). Local

seismographs and accelerographs (triangles) are also shown. Faults after Ganas et al. (2013). The beachball represents the focal mechanism of the 2020 Samos mainshock. The inset map shows the location of the study area (red rectangle) in the context of major tectonic structures, such as the subduction zone (Hellenic Arc) and the North Anatolian Fault (NAF). The location of Lesbos (L) and Kos (K) islands are also marked on the inset map

study the anisotropic properties of the crust in the immediate area of the mainshock.

Data and methodology

The recent seismic sequence of the $M_w = 6.9$ mainshock provided a substantial amount of recorded data. However, since this dataset is temporally constrained (between 2020/10/30 and 2020/11/30), we retrieved further events and waveforms from the previous five years (i.e., since 2015/01/01), to establish a background of anisotropy. Event and phase arrival information were acquired from the European and Mediterranean Seismological Centre (EMSC) for the period between 2015/01/01 and 2018/07/31, the public catalogue of the Seismological Laboratory of the National and Kapodistrian University of Athens (SL-NKUA) between 2018/06/01 and 2020/10/29 and a seismic catalogue of the first month of the 2020 Samos aftershock sequence, compiled from the bulletins of SL-NKUA and GI-NOA, part of which was presented in Papadimitriou et al. (2020). Our final catalogue consisted of 1,376 seismic events in the vicinity of the island. Seismicity in the area is generally constrained in the crust, with the majority of the foci located shallower than 15 km. Four stations that were operational before the mainshock (GMLD, KRL1, KUSD and SMG) and two temporary

stations installed after the event (SAM1 and SAM2) were available. As expected, almost half of the considered events (647) were part of the 2020 sequence.

It is noted that we used recordings by both seismographs (SAM1, SAM2 and SMG) and accelerographs (GMLD, KRL1 and KUSD). Thus, raw recordings were first very broadly filtered between 0.005 and 50.0 Hz, the instrument response was removed and, in the cases of accelerographs, were integrated to velocity. Preprocessing was carried out using the ObsPy package (Krischer et al. 2015). All waveform data were acquired through the international Federation of Digital Seismograph Networks' (FDSN) service from the European Integrated Data Archive (EIDA) nodes at KOERI-RETMC (<https://www.orfeus-eu.org/data/eida/nodes/KOERI/>) for stations GMLD and KUSD and GI-NOA (<http://eida.gein.noa.gr/webdc3/>) for KRL1, SAM1, SAM2 and SMG.

To eliminate unsuitable arrivals at candidate stations, the “shear-wave window” criterion (Evans 1984) was enforced. The interaction of shear-waves with the free surface can generate secondary arrivals (e.g., converted pS phases) which need to be avoided during analysis. As such, a maximum incidence angle of the seismic ray is used to exclude such incidents. This threshold (i.e., the “shear-wave window”) was set to 45.0° , per previous studies (e.g., Gao et al. 2011; Kaviris et al. 2017). The incidence angle for each candidate ray was estimated during the analysis with the TauP algorithm

(Crotwell et al. 1999). This necessary step, to ensure the quality of the final dataset, severely reduced the number of available data to 262 event-station pairs. However, it accurately represents the scarcity of events in the close vicinity of the stations (Fig. 1). Moreover, low Signal-to-Noise Ratio (SNR) recordings were also rejected. The SNR limit was set to 1.5, after manually reviewing waveforms with the splitting software described in the next paragraph.

The analysis for shear-wave splitting was carried out with the Pytheas software (Spingos et al. 2020). The processing algorithm of choice was the Eigenvalue method (Silver and Chan 1991) with the automation introduced by Teanby et al. (2004). These methods are frequently used in SwS analysis and have been integrated in multiple software tools in the past (Illsley-Kemp et al. 2017; Johnson and Savage 2012; Nolte et al. 2017). To improve on the quality of the measurements, two additional algorithms were used through Pytheas. First, for each waveform set, a bandpass filter had to be applied to remove the noise content. The boundaries of the filter were automatically selected with the process described in Savage et al. (2010). Second, a quality grade had to be assigned to measurements, to identify spurious and ambiguous cases. The grading algorithm (Spingos et al. 2020) uses a combination of three criteria; (a) the error of φ , (b) the error of t_d and (c) the correlation coefficient between shear-waves in the two horizontal components, after the removal of the anisotropy's effect. Given grades range from "A" (best) to "E" (worst). Furthermore, in cases where φ was either (sub)parallel or (sub)perpendicular to p , a special grade ("N") denoting null (Wüstefeld and Bokelmann 2007) measurements was provided by the algorithm. The overall processing scheme is detailed in Appendix 1.

Results

In total, 262 splitting measurements were produced. However, after considering observations of sufficient quality (only those graded "C" or better) and excluding null measurements, we obtained a final catalogue of 164 anisotropy

results. Out of the six initially considered stations, two of them yielded no results of satisfying quality (i.e., KUSD and SAM1). A summary of the average splitting parameters for the stations with reliable results (i.e., GMLD, KRL1, SAM2 and SMG) is presented below (Table 1). Since φ observations are directional, we used circular statistics (Berens 2009) to account for wrapping of polarization directions.

Station SMG displays a clear WNW-ESE polarization direction of the S_{fast} , perpendicular to the ones observed in the other three stations (Fig. 2a). KRL1 has a dominant NE-SW average φ , which is intersected by a secondary perpendicular direction. However, in contrast to SMG, φ observations at KRL1 are more scattered. GMLD has a very small count of observations (4), while SAM2 has the second smallest number of results (15). In general, as errors in Table 1 suggest, the behavior of φ is better constrained in KRL1 and SMG, i.e., in the stations where the vast majority (88.4%) of the SwS results was obtained. Average time-delays generally deviate around the 90.0 ms mark, with the exception of SAM2. Normalized time-delays, i.e., time-delays normalized per the hypocentral distance, follow a similar pattern Table 1, being around 6.0 ms/km in GMLD, KRL1 and SMG. Errors for the latter were calculated using the formulation proposed by Del Pezzo et al. (2004), to integrate uncertainties of the source-receiver distance estimation. Regarding the azimuthal distribution, as the majority of the analyzed events belong to the 2020 sequence, results are mostly constrained to the N-NE for the three stations on the island. Only SMG offers some insight, where odd measurements of φ are present all around the station, suggesting no correlation of deviating polarization directions with specific ray paths (Fig. 2b).

The processing of the data yielded a total of 27 null observations, among three of the four stations (KRL1, SAM2, SMG), with the majority observed at KRL1 (21 measurements). Polarization directions of null measurements follow a general NW-SE trend, which does not agree with either the regional stress regime or the local tectonic structures.

Table 1 Summary of statistics for the shear-wave splitting analysis

Station	Network	N	$\bar{\varphi} \pm \delta\bar{\varphi} (N^\circ E)$	$\bar{t}_d \pm \delta\bar{t}_d (ms)$	$\bar{t}_n \pm \delta\bar{t}_n \left(\frac{ms}{km}\right)$
All stations	All networks	164	77.5 ± 4.0	95.6 ± 4.4	6.7 ± 0.4
GMLD	KO	4	65.4 ± 10.0	87.5 ± 34.2	5.8 ± 1.2
KRL1	HI	90	54.4 ± 5.0	92.1 ± 5.8	6.8 ± 0.6
SAM2	HL	15	34.7 ± 12.7	133.3 ± 16.2	9.2 ± 1.9
SMG	HL	55	107.2 ± 4.8	91.6 ± 7.4	5.9 ± 0.7

The number of observations (N), mean value and the corresponding standard error of mean (δ) are included. The table displays values for the polarization direction (φ), the time-delay (t_d) and the normalized time-delay (t_n)

KO Kandilli Observatory and Earthquake Research Institute (KOERI, <https://doi.org/10.7914/SN/KO>), HI Institute of Engineering Seismology and Earthquake Engineering (ITSAK, <https://doi.org/10.7914/SN/HI>), HL National Observatory of Athens (NOA, <https://doi.org/10.7914/SN/HL>)

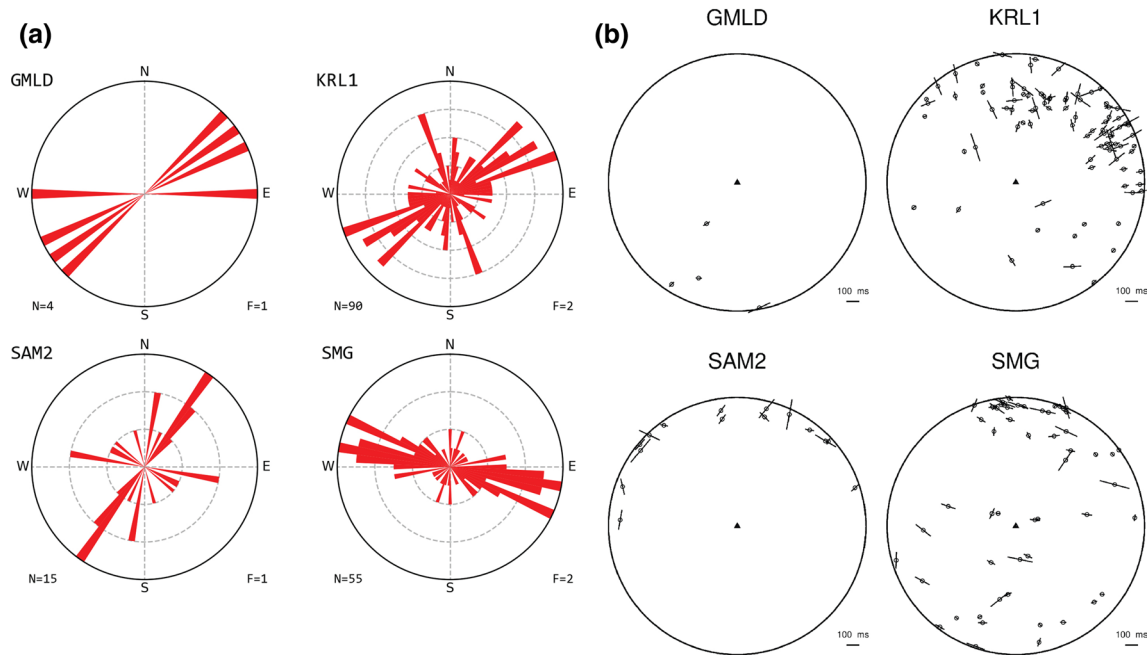


Fig. 2 **a** Rose diagrams displaying the distribution of φ for each station. N is the total number of observations and F the count of measurements per grid line. **b** Equal-area projections of individual splitting observations per station (triangle at the center). The circle's

radius indicates an angle of incidence equal to the shear-wave window (45°). The length of each vector is proportionate to the respective t_d

Moreover, nulls at KRL1 are perpendicular to S_{fast} , indicating some coherence with expected S_{slow} polarization directions. We cannot comment on the other two stations due to the very small number of observations in either SAM2 (2) or SMG (4). Summary plots of the null results are presented in Appendix 2.

Discussion

The analysis revealed, for the first time, that the upper crust at the Samos Island is anisotropic. However, attributing the origin of anisotropy to either stress or structures is paramount for understanding the mechanics behind the phenomenon and determining the implications of the measured splitting parameters. In the following, we attempt to distinguish between the two possible causes of anisotropy, constrained by the limited available data.

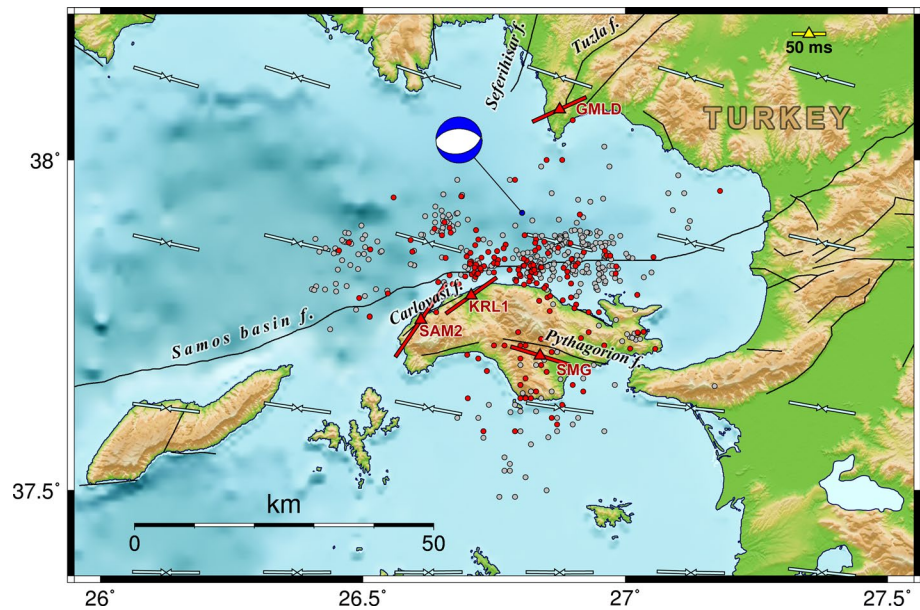
Source of anisotropy at Samos Island

As mentioned above, shear-wave splitting is a phenomenon commonly associated with crustal microcracks (Crampin 1994; Crampin et al. 1980; Crampin and Peacock 2005; Margheriti et al. 2006). This association is generally supported by observed polarization directions of the S_{fast} being approximately parallel to the regional maximum horizontal

stress component S_{Hmax} . Evidence of a microcrack-filled upper crust have significant connotations; if we can reliably sample changes in microcrack features from shear-wave splitting, we can associate them with an impending earthquake (Crampin et al. 1999, 2015). However, SwS phenomena can also originate from local tectonic structures. This case can be identified by φ directions parallel to the axes of rock characteristics. Structurally-controlled anisotropy has been observed globally in various environments (Cochran et al. 2003, 2006; Graham et al. 2020; Hiramatsu et al. 2010; Shi et al. 2020; Zinke and Zoback 2000). Differentiating between a microcrack-dominant and a structurally-controlled anisotropy state can be an arduous task; if the S_{Hmax} is parallel to the fault lines (as in the case of tectonic environments with pure normal dip-slip focal mechanisms) it is almost impossible to make such a distinction (Pastori et al. 2019).

The regional deformation characteristics compose a trans-tensional stress regime in the eastern Aegean Sea. The dominant active structures in the region of Samos Island, such as the Samos Basin fault (e.g., Ganas et al. 2013), just offshore to the north, are E-W trending normal faults, shaping the main morphology of Samos Island, the basins, but also the mountains at the opposite coast of Turkey. However, strike-slip faulting is also present in the region, evident from the focal mechanisms of recent seismicity (Benetatos et al. 2006; Tan et al. 2014; Yolsal-Çevikbilen et al. 2014). Along the north-western coast of the island, the NE-SW trending,

Fig. 3 Average S_{fast} polarization directions (red lines) for each station (triangles). The length of each vector is proportionate to the average time-delay at the station. Red circles show events with at least one shear-wave splitting result, whereas gray circles represent events with all-rejected measurements. Cyan arrows indicate the orientation of S_{Hmax} , after Kapetanidis and Kassaras (2019). The focal mechanism of the 2020 $M_w=6.9$ event is also shown. Rest of notation as in Fig. 1



north-dipping Carlovasi fault exhibits dextral strike-slip faulting, whereas the roughly WNW-ESE-trending, south-dipping Pythagorion fault, further to the SE, is characterized by normal kinematics (Chatzipetros et al. 2013). The NE-SW faulting trend is further extended westwards, emphasized on a regional scale by the 250 km-long Samos Basin normal fault feature, spanning from western Turkey to the middle of Central Aegean Sea (Ganas et al. 2013; Kreemer and Chamot-Rooke 2004). Samos Island also hosts a stack of several nappes and thrusts, the latter mainly striking NW–SE to N–S (Ring et al. 2007), with a strong presence of metamorphic rocks (Stamatakis et al. 2009). The nearby coast of Turkey is dominated by complex structures (east of the island) and NNE–SSW trending faults, north of Samos (Ocakoglu et al. 2005).

Our results (Fig. 3) seem to follow the strike of faults in the area. KRL1 and SAM2, located to the NW, present similar orientations to the Carlovasi fault. The average φ value in SMG is parallel to the Pythagorion fault's strike. GMLD presents a different polarization direction than the strike in Seferihisar and Tuzla faults, but the small number of observations in the station cannot offer a reliable picture of splitting there. According to the above, two stations (KRL1 and SAM2) present a φ value that is very different from the orientation of the S_{Hmax} , which offers strong evidence for a state of structurally-controlled anisotropy in Samos. Additionally, co-seismic deformation measured at nearby GNSS stations showed similarly oriented horizontal ground displacement vectors, with a direction of approximately N190°E (V. Sakkas, personal communication). The mean anisotropy direction in station SMG is also parallel to

the local fault line, but parallel to S_{Hmax} as well, which does not allow for a clear interpretation.

Temporal evolution of splitting parameters

To identify whether changes of polarization directions or time-delays with time exist in our case, we explored variations of the estimated splitting parameters, i.e., φ and normalized time-delays (t_n), for the two stations that offered an adequate number of observations, i.e., KRL1 and SMG. Temporal variations are a common point of discussion in shear-wave splitting studies (e.g., Piccinini et al. 2006). According to literature, rays that travel within a solid angle between 15° and 45° to the microcrack plane are more sensitive to stress variations; these rays are classified in “Band-1”, while the ones that propagate through a solid angle narrower than 15° belong to “Band-2” (Crampin et al. 1999). In the following, we present the five-year temporal evolution of the splitting parameters in all three categories (“all bands”, “Band-1” and “Band-2”) for each station.

Polarization directions in KRL1 (Fig. 4a, c) are generally affected by the extent of their scattering (Fig. 2a). In the five-year interval between 2015 and 2020 (Fig. 4a), the observed changes in φ are not correlated with the occurrence of a strong seismic event. A few outliers, which exist between N120°E and N180°E, appear only circumstantially. Abrupt changes by 90° in φ (the so-called 90°-flips) have been attributed to increased pore pressure in rocks and have been observed primarily in volcanic areas due to rays passing either through or near magmatic bodies, such as dykes

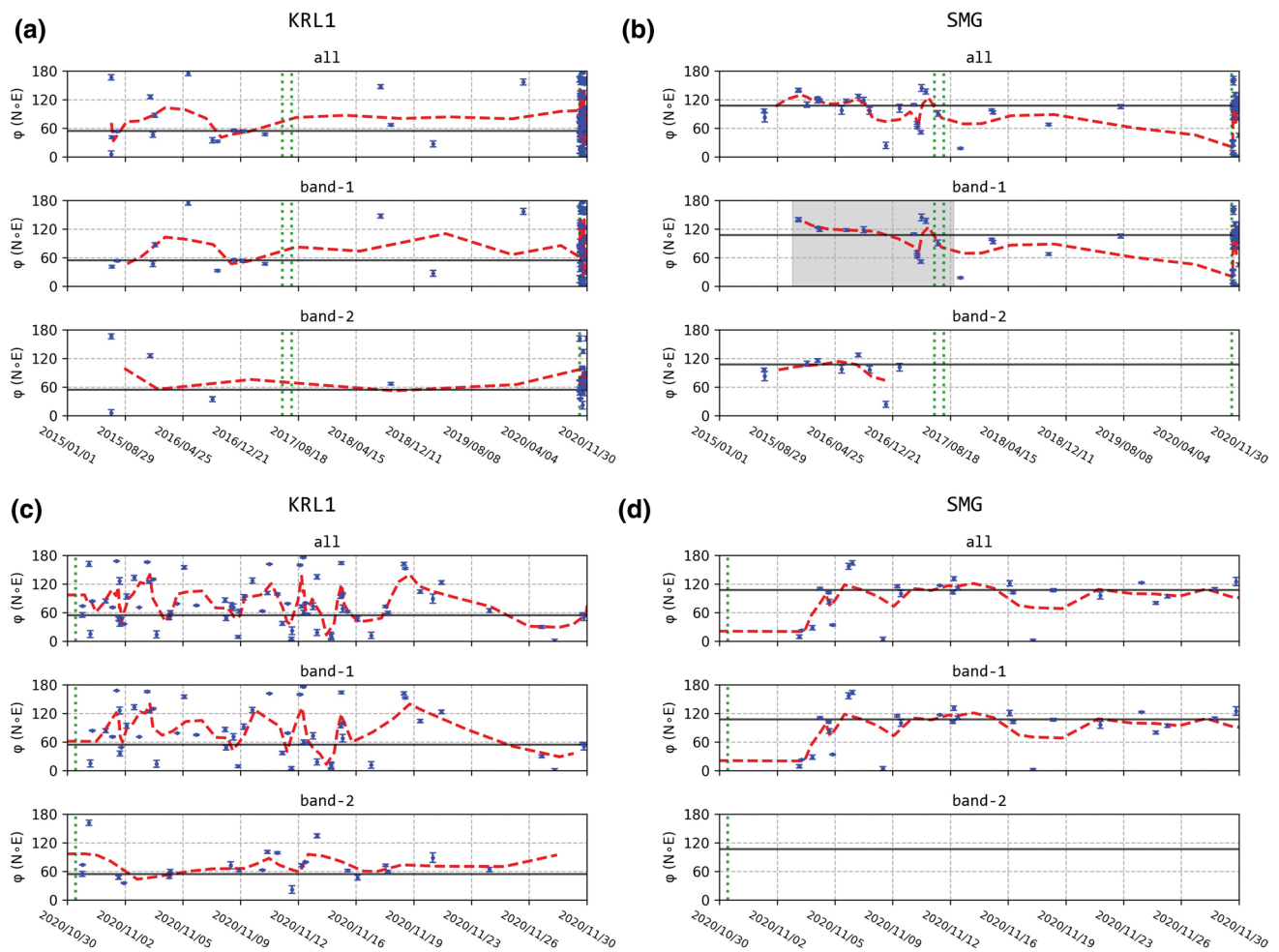


Fig. 4 Variations of φ between 2015 and 2020 (**a, b**) and for the aftershock sequence between 2020/10/30 and 2020/11/30 (**c, d**) for stations KRL1 (**a, c**) and SMG (**b, d**). In each panel, observations classified as “all-bands” (top), “band-1” (middle) and “band-2” (bottom) are presented, respectively. Each data point is represented by a circle with its corresponding error. The bold red dashed line indicates the

three-point moving average. The horizontal black solid line denotes the average φ , as exhibited in (Table 1). The vertical green dotted lines note the origin times of earthquakes with $M \geq 5.5$ in epicentral distances of approximately up to 150 km. The shaded area in (**b**) is detailed in Fig. 6b

(e.g., Johnson et al. 2011; Unglert et al. 2011). High pressure of pore-fluids which is not related to volcanism can also result in this phenomenon; increased pore pressure on the fault causes flips to microcracks adjacent to it, while the polarization direction recorded at the station is affected gradually by the propagation medium away from the source (Crampin et al. 2002). Consequently, as the resulting φ is affected by different causes, its per station distribution is rendered complicated (Gao et al. 2011, 2019; Crampin and Gao 2014). Such a phenomenon could be the cause of the significant scattering we observe in KRL1, especially during the aftershock sequence (Fig. 4c). KRL1 is located almost next to the causative fault (Papadimitriou et al. 2020) of the 2020 event (Samos basin f., Fig. 3) and, consequently, the observation of flipped φ due to high pore pressure on the

fault is more likely. SMG showcases a temporal distribution of φ generally constrained around its average value (Fig. 4b), before 2020, with the occasional outlier. On the other hand, observations related to the aftershock sequence (Fig. 4d) indicate an initially flipped φ until 2020/11/03 which then reverts to its prior state. A possible explanation is the release of tectonic stress due to the mainshock. As time progresses and the release of seismic energy is expressed through aftershocks, the stress is reduced. Thus, the zone (and as such, the microcracks) affected by the pressure buildup on the fault is reduced. As SMG is located further away from the aftershocks zone, seismic rays are travelling at a greater distance away from the source (as opposed to KRL1) and are affected more by the intermediate propagation medium.

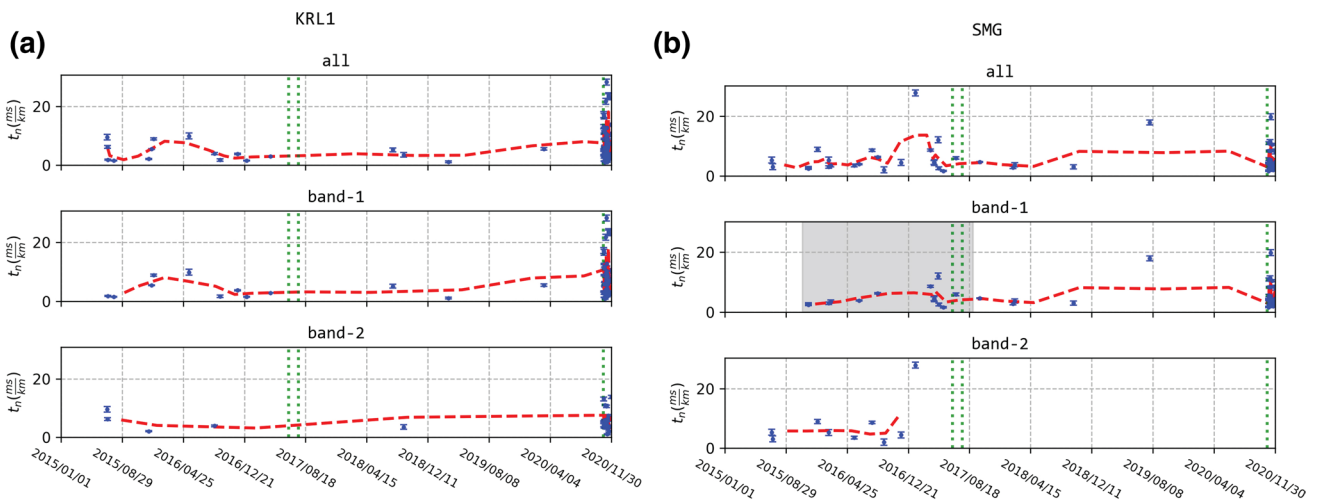


Fig. 5 Variations of normalized time-delays between 2015 and 2020 for stations KRL1 (a) and SMG (b). The shaded area in “band-1” of panel (b) denotes the time period shown in Fig. 6. Other notation as in Fig. 4

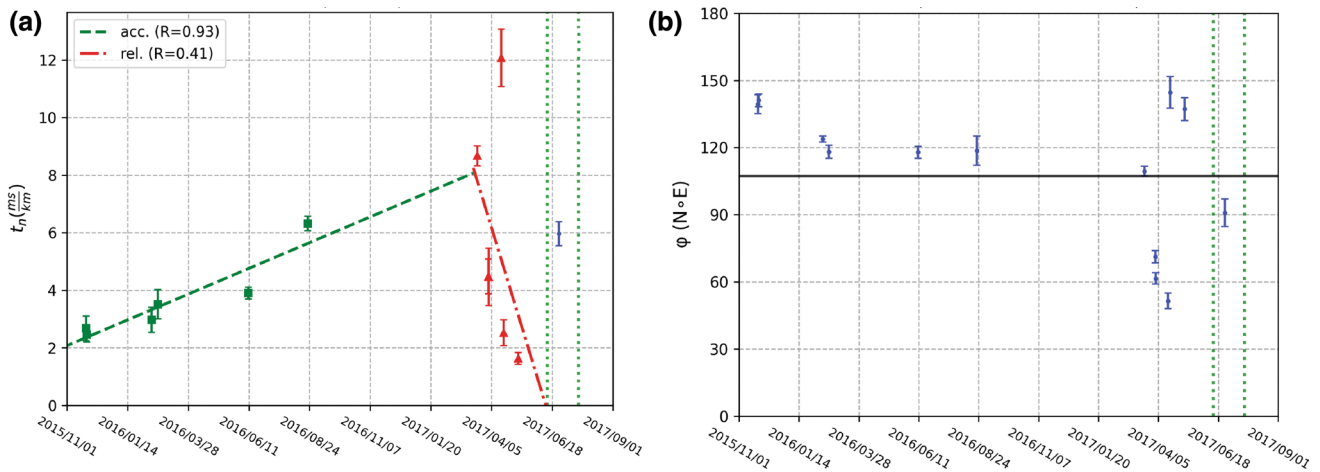


Fig. 6 Variations of t_n (a) and ϕ (b) of “band-1” observations, between 2015/11 and 2017/09, for station SMG. In (b), the suggested stress accumulation (green dashed line) and relaxation (red dashed-dotted line) are shown. The linear models have been determined by regression analysis using the least squares method with t_n data points

Concerning the variations of t_n , a decrease is observed in KRL1 before 2016/04, which follows a suggested period of increasing time-delays (Fig. 5a). Examining measurements that belong exclusively to “Band-1” pronounces this change. Concerning the recent $M_w = 6.9$ event, the few data points between 2016/12 and 2020/10 do not permit the extrapolation of solid conclusions. An increase is observed in the running mean after 2019/08, but it is strongly biased by the scattered measurements associated with the aftershock sequence and cannot be considered indicative of any physical process. Nevertheless, it is noteworthy that individual

exhibiting increase (green squares) or decrease (red triangles). A single high- t_n point ($t_n > 12$ ms) greatly affects the relaxation model, as highlighted by the much smaller correlation coefficient (R). Other notation as in Figs. 4 and 5

t_n values are less than 20 ms/km, in the five-year period preceding the mainshock. In SMG station (Fig. 5b), changes are similarly ambiguous. Examining all data, a clear increase and decrease can be observed between 2016/08 and 2017/04. However, this variation is much weaker in “Band-1”; this is a result of the individual high (over 20 ms/km) t_n being classified to “Band-2”. A mean increase, affected by the scattering of time-delays of the aftershock sequence, is then observed. However, in this case, time-delay values are generally constrained below 20 ms/km, even for measurements from the 2020 sequence events. In contrast, KRL1, which is

closer to the epicenter of the mainshock, exhibited a significant number of high t_n values in the same period.

At first glance, the number of observations in either case is not adequate to draw reliable conclusions. We searched the seismic catalogue of NKUA-SL for strong earthquakes ($M_w \geq 5.5$) to find possibly associated events, in a radius of 150 km from Samos; shorter distances have been reported in the literature, for weaker events (e.g., Gao and Crampin 2006). Other than the recent 2020 $M_w = 6.9$ event, there are two large shocks in the broader area; (a) the 2017/06 Lesvos earthquake of $M_w = 6.3$ (Kiratzi, 2018; Papadimitriou et al. 2018) at an approximate distance of 130 km and (b) the Kos $M_w = 6.6$ event, which occurred a month later on 2017/07 (Ganas et al. 2019), 100 km away from the island (see Fig. 1 for the locations of Lesvos and Kos islands). Variations in KRL1 (Fig. 5a) seem to be unrelated to the above events. The increase and drop of time-delays is recorded over half a year before. However, there is evidence for a connection between the occurrence of the 2017 Aegean earthquakes and variations in SMG (Fig. 6a). The observation of a t_n increase period (T_i), indicating stress accumulation, starting from 2015/11 and lasting for 556 days is documented, with a regression correlation coefficient (R) equal to 0.93. It is followed by a decrease period (T_r), suggesting stress relaxation (Gao and Crampin 2004) of 90 days, with a worse $R = 0.41$. The time periods selected for the regression analysis were obtained from the proposed relations of Crampin et al. (2013), for a $M_w = 6.3$ event. We do not have enough data to investigate changes associated with a $M_w = 6.6$ earthquake, which would correspond to $T_i = 766$ days and $T_r = 164$ days. If this is the case, then SMG might indeed sample an anisotropic space where stress-sensitive microcracks are prevalent. Temporal changes of φ at SMG seem to be concentrated before the 2017/06 event (Fig. 6b). A group of three $\sim N60^\circ E$ is followed by two $\sim N140^\circ E$ measurements. However, we do not believe these can be associated with the event, which is located 130 km away; rays analyzed for anisotropy are not affected by the distant fault (and its adjacent microcracks of varying orientation) at Lesvos. Further work is required to comprehend their relation to local tectonic processes.

Conclusions

The recent $M_w = 6.9$ Samos event and its seismic sequence was a unique opportunity to study the anisotropic properties of the upper crust in the area, due to the provision of a high number of earthquakes located close to local seismographs and accelerographs. Automatic analysis of

data from the island and its neighboring mainland offered new perspectives on the state of crustal anisotropy. Average polarization directions of the S_{fast} are generally aligned according to local faults, irrespective of the regional S_{Hmax} . This is strong evidence supporting a mechanism of anisotropy dominated by local structures. However, measurements at station SMG, located in the southern part of the island, where the local Pythagorion fault is oriented according to the S_{Hmax} , perplex the situation, as it is not possible to distinguish between the two anisotropy sources, from φ alone.

Changes of φ were observed during the aftershock sequence, possibly due to the pressure buildup near the causative fault, with the scattering of φ being more pronounced in the station closer to the fault, i.e., KRL1. Variations of normalized time-delays exhibited some evidence of association with seismic events at larger distances. Namely, an $M_w = 6.3$ which occurred at 130 km away from Samos on 2017/06, followed by an $M_w = 6.6$ on 2017/07, at a distance of 100 km. These changes, related to stress accumulation and relaxation, are observed in SMG. If we accept that the variations of time-delays are indeed a prelude to the 2017/06 event, which is statistically (although not robustly) supported as shown in Fig. 6, then this station seems to sample a stress-controlled anisotropic space and its average φ is aligned according to S_{Hmax} . However, this behavior is not well-documented, as the associated data points are few. The Samos event would be a great opportunity to support this, since the epicenter is located in the vicinity of the station, but there were not enough data before its occurrence. Future work on the area should focus on the period preceding this earthquake, by conducting a more detailed microseismic analysis to enrich the catalogue of suitable events. In any case, the absence of significant time-delay temporal variations in KRL1 and its existence in SMG, along with their difference in polarization direction, might suggest a structurally-controlled origin of anisotropy to the NW and a dominant effect of stress to the SE.

As the area of the Eastern Aegean has shown from the activity in the past two years, a densification of the local networks would greatly enhance our ability to study seismic anisotropy in the region, identify the mechanism of SwS and recognize potential time-delay variations as precursors.

Appendix 1–Shear-wave splitting processing

To process as many station-event pairs as possible and remove user bias during the analysis, we employed a fully automatic process using the Pytheas software (Spingos

Fig. 7 Summary report of the Eigenvalue method, showcasing the waveforms (a) and particle motion diagrams (b) before and after the removal of the splitting effect. The optimal signal window selected through cluster analysis is represented by the shaded area. The contour plot (c) displays the variation of the minimum eigenvalue (λ_2) of the radial and transverse components covariance matrix after the removal of anisotropy, with the crosshair indicating the minimum value and the 95% confidence interval outlined (bold contour). Note the linearization of the particle motion in the NE plane, after the removal of splitting (panel b, bottom)

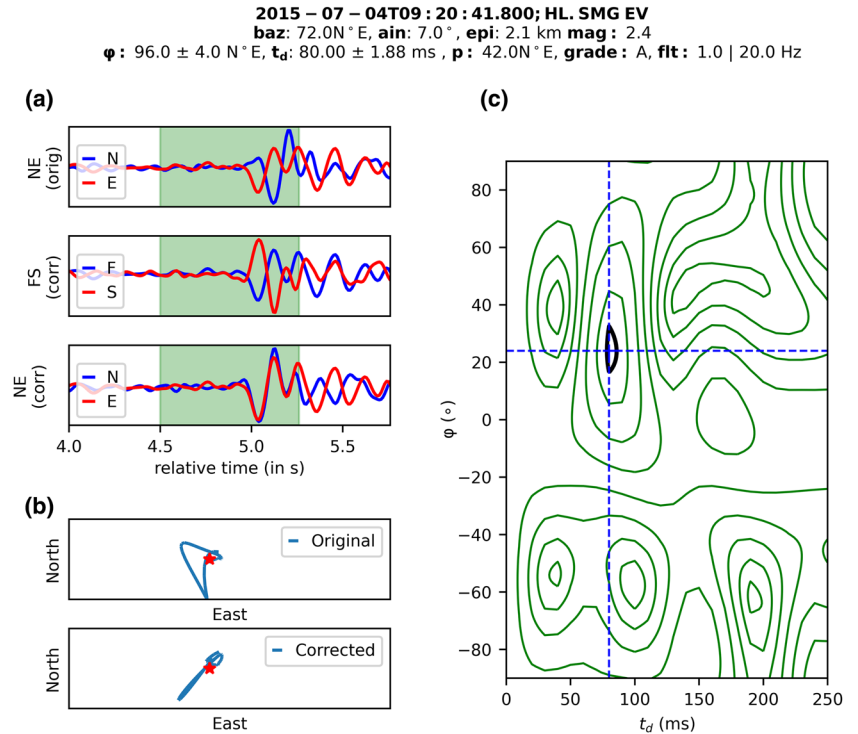
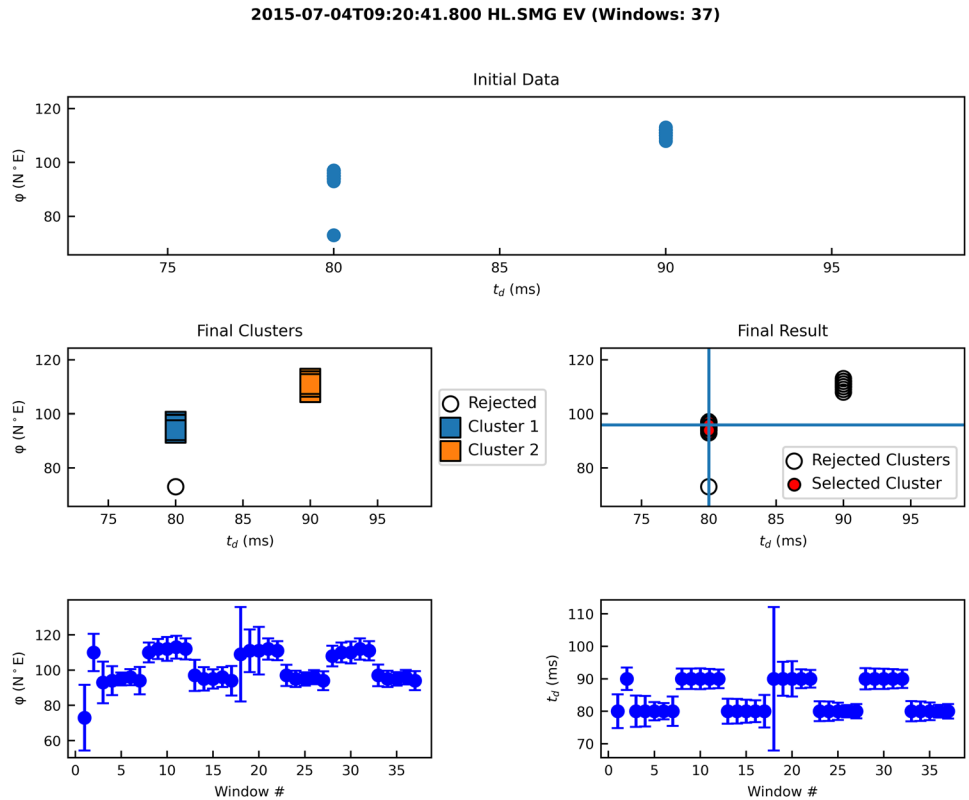


Fig. 8 Summary of the results of cluster analysis for 37 candidate signal windows. Top: the initial space of ϕ and t_d observations used in clustering. Middle: clusters of measurements (left) as obtained by the algorithm and selection of the final cluster and measurement, as indicated by the crosshair (right). Bottom: variation of ϕ (left) and t_d (right) per index number of candidate signal window. The bottom plots essentially showcase the stability of either parameter with differing windows



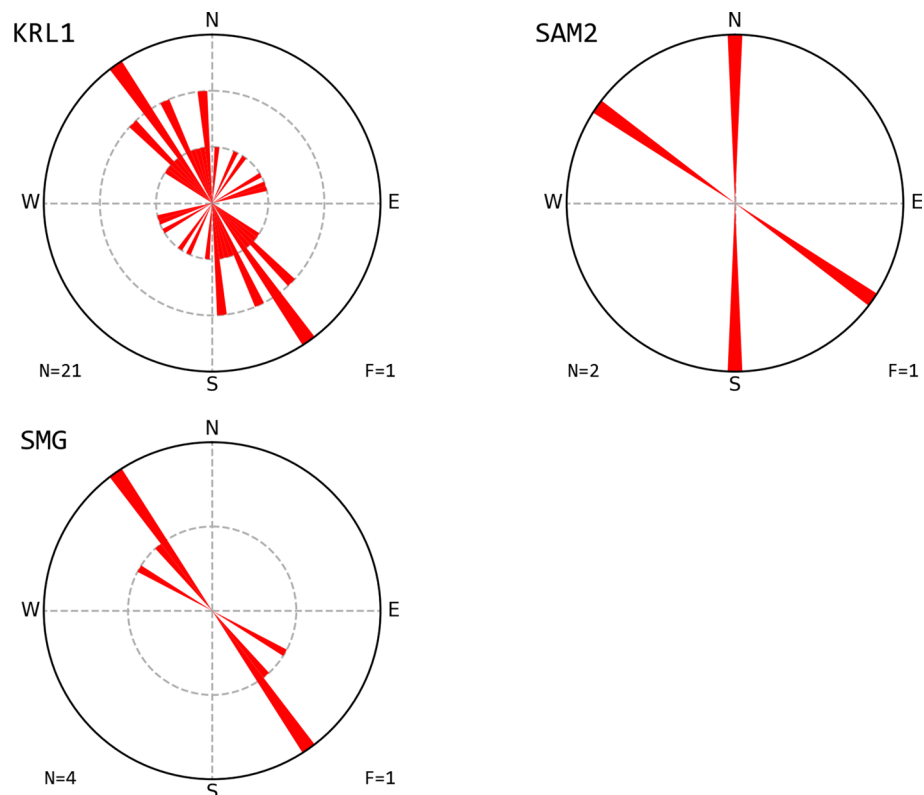
et al. 2020). As a first preprocessing scheme, a series of user-predefined band-pass filters were applied to the initial waveforms and the one yielding the highest SNR was selected (Savage et al. 2010). The Eigenvalues (EV) method of Silver and Chan (1991) performs a series of shear-wave splitting corrections based on different combinations of φ and t_d . For each set of parameters, the covariance matrix of the two horizontal components, after correction, is obtained and the second, minimum, eigenvalue (λ_2) is extracted. The φ and t_d pair that yielded the lowest λ_2 is considered as the optimal measurement. In Fig. 7 we present an example of the analysis with the EV method. In the selected signal window (see next paragraph for its automated selection) the particle motion was linearized after correcting for anisotropy. Moreover, Silver and Chan (1991) offered a comprehensive error estimation system. However, Walsh et al. (2013) identified an underestimation in the original system and proposed new formulations which resolved the issue. We followed the formulations of the latter.

To automatically select the signal window analyzed by the EV method, we adopted the Teanby et al. (2004) approach, which utilizes cluster analysis (Fig. 8). In brief, EV is first applied to a prefixed range of candidate signal windows. Then, clusters are hierarchically formed in the initial space of φ and t_d observations. Then, the number of optimal clusters is estimated and, consequently, the most constrained cluster is identified. Out of the latter, the observation pair with the minimum errors corresponds to the optimal signal window.

Appendix 2–Null measurements

In the following, we present rose diagrams for all measurements graded as “null” (Fig. 9). SAM2 and SMG stations exhibit only a few null measurements. KRL1 showcases a dominant NW–SE direction of null measurements. This is similar to the direction of possibly flipped microcracks near the causative fault of the 2020 Samos earthquake, as discussed in the main text.

Fig. 9 Rose diagrams displaying the distribution of φ for each station, for observations characterized as “null”. N is the total number of observations and F the count of measurements per grid line



Supplementary information The online version contains supplementary material available at <https://doi.org/10.1007/s11600-021-00598-2>.

Acknowledgments We are very grateful to the personnel of all institutions involved in the installation, operation and maintenance of the seismographs and accelerographs located at and around the island of Samos. We would also like to thank Dr. Vasileios Sakkas for providing recent unpublished GNSS data. Our gratitude is expressed to Dr. Lucia Margheriti and an anonymous reviewer, for their constructive criticism on the article. Maps were created with the General Mapping Tools software (Wessel et al. 2019). Other figures were plotted with Matplotlib (Hunter 2007). The Pytheas software for shear-wave splitting analysis can be downloaded freely from <https://github.com/ispin-gos/pytheas-splitting>.

Authors' contribution All authors have participated in all stages required for the preparation, writing and publication of the article.

Funding We acknowledge support of this study by the project “HEL-POS – Hellenic Plate Observing System” (MIS 5002697) which is implemented under the Action “Reinforcement of the Research and Innovation Infrastructure”, funded by the Operational Programme “Competitiveness, Entrepreneurship and Innovation” (NSRF 2014–2020) and co-financed by Greece and the European Union (European Regional Development Fund).

Declarations

Conflict of interest The authors have no conflicts of interest to declare that are relevant to the content of this article.

References

- Ambraseys N (2015) Earthquakes in the Mediterranean and Middle East: A multidisciplinary study of seismicity up to 1900. Cambridge Univ Press. <https://doi.org/10.1017/CBO9781139195430>
- Aster RC, Shearer PM, Berger J (1990) Quantitative measurements of shear wave polarizations at the Anza Seismic Network, southern California: Implications for shear wave splitting and earthquake prediction. *J Geophys Res* 95:12449. <https://doi.org/10.1029/JB095iB08p12449>
- Benetatos C, Kiratzi A, Ganas A, Ziazia M, Plessa A, Drakatos G (2006) Strike-slip motions in the Gulf of Sığaçık (western Turkey): Properties of the 17 October 2005 earthquake seismic sequence. *Tectonophysics* 426:263–279. <https://doi.org/10.1016/j.tecto.2006.08.003>
- Berens P (2009) CircStat: a MATLAB toolbox for circular statistics. *J Stat Softw* 31:1–21
- Bernard P, Chouliaras G, Tzanis A, Briole P, Bouin MP, Tellez J, Stavrakakis G, Makropoulos K (1997) Seismic and electrical anisotropy in the Mornos delta, Gulf of Corinth, Greece, and its relationship with GPS strain measurements. *Geophys Res Lett.* <https://doi.org/10.1029/97GL021102>
- Bianco F, Zaccarelli L (2008) A reappraisal of shear wave splitting parameters from Italian active volcanic areas through a semi-automatic algorithm. *J Seismol* 13:253–266. <https://doi.org/10.1007/s10950-008-9125-z>
- Boness NL, Zoback MD (2006a) A multiscale study of the mechanisms controlling shear velocity anisotropy in the San Andreas Fault Observatory at Depth. *Geophysics* 71:F131–F146. <https://doi.org/10.1190/1.2231107>
- Boness NL, Zoback MD (2006b) Mapping stress and structurally controlled crustal shear velocity anisotropy in California. *Geology* 34:825–828. <https://doi.org/10.1130/G22309.1>
- Bouin MP, Tellez J, Bernard P (1996) Seismic anisotropy around the Gulf of Corinth, Greece, deduced from three-component seismograms of local earthquakes and its relationship with crustal strain. *J Geophys Res Solid Earth* 101:5797–5811. <https://doi.org/10.1029/95JB03464>
- Brun J, Faccenna C, Gueydan F, Sokoutis D, Philippon M, Kydonakis K, Gorini C (2016) Effects of slab rollback acceleration on Aegean extension. *Bull Geol Soc Greece* 50:5–14
- Chatzipetros A, Kiratzi A, Sboras S, Zouros N, Pavlides S (2013) Active faulting in the north-eastern Aegean Sea Islands. *Tectonophysics* 597–598:106–122. <https://doi.org/10.1016/j.tecto.2012.11.026>
- Cochran ES, Vidale JE, Li YG (2003) Near-fault anisotropy following the Hector Mine earthquake. *J Geophys Res Solid Earth.* <https://doi.org/10.1029/2002jb002352>
- Cochran ES, Li YG, Vidale JE (2006) Anisotropy in the shallow crust observed around the San Andreas fault before and after the 2004 M 6.0 Parkfield earthquake. *Bull Seismol Soc Am* 96:364–375. <https://doi.org/10.1785/0120050804>
- Crampin S (1994) The fracture criticality of crustal rocks. *Geophys J Int* 118:428–438. <https://doi.org/10.1111/j.1365-246X.1994.tb03974.x>
- Crampin S, Evans R, Üçer B, Doyle M, Davis JP, Yegorkina GV, Miller A (1980) Observations of dilatancy-induced polarization anomalies and earthquake prediction. *Nature* 286:874–877. <https://doi.org/10.1038/286874a0>
- Crampin S, Volti T, Chastin S, Gudmundsson A, Stefánsson R (2002) Indication of high pore-fluid pressures in a seismically-active fault zone. *Geophys J Int* 151(2):F1–F5. <https://doi.org/10.1046/j.1365-246X.2002.01830.x>
- Crampin S, Gao Y, Bukits J (2015) A review of retrospective stress-forecasts of earthquakes and eruptions. *Phys Earth Planet Inter* 245:76–87. <https://doi.org/10.1016/j.pepi.2015.05.008>
- Crampin S, Gao Y, De Santis A (2013) A few earthquake conundrums resolved. *J Asian Earth Sci* 62:501–509. <https://doi.org/10.1016/j.jseaes.2012.10.036>
- Crampin S, Peacock S (2005) A review of shear-wave splitting in the compliant crack-critical anisotropic Earth. *Wave Motion* 41:59–77. <https://doi.org/10.1016/j.wavemoti.2004.05.006>
- Crampin S, Volti T, Stefánsson R (1999) A successfully stress-forecast earthquake. *Geophys J Int* 138:F1–F5. <https://doi.org/10.1046/j.1365-246x.1999.00891.x>
- Crampin S, Zatsepin S (1997) Modelling the compliance of crustal rock—II. Response to temporal changes before earthquakes. *Geophys J Int* 129:495–506. <https://doi.org/10.1111/j.1365-246X.1997.tb04489.x>
- Crampin S, Gao Y (2014) Two species of microcracks. *Appl Geophys* 11:1–8. <https://doi.org/10.1007/s11770-014-0415-7>
- Crotwell HP, Owens TJ, Ritsema J (1999) The TauP Toolkit: Flexible Seismic Travel-time and Ray-path Utilities. *Seismol Res Lett* 70:154–160. <https://doi.org/10.1785/gssrl.70.2.154>
- Del Pezzo E, Bianco F, Petrosino S, Saccorotti G (2004) Changes in the coda decay rate and shear-wave splitting parameters associated with seismic swarms at Mt. Vesuvius. *Italy Bull Seismol Soc Am* 94:439–452
- Durand S, Montagner JP, Roux P, Brenguier F, Nadeau RM, Ricard Y (2011) Passive monitoring of anisotropy change associated with the Parkfield 2004 earthquake. *Geophys Res Lett.* <https://doi.org/10.1029/2011GL047875>
- Evangelidis CP (2017) Seismic anisotropy in the Hellenic subduction zone: Effects of slab segmentation and subslab mantle flow. *Earth Planet Sci Lett* 480:97–106. <https://doi.org/10.1016/j.epsl.2017.10.003>
- Evangelidis CP, Triantafyllis N, Samios M, Boukouras K, Kontakos K, Ktenidou O-J, Fountoulakis I, Kalogeras I, Melis N, Galanis O, Papazachos C, Hatzidimitriou P, Scordilis E, Sokos E, Parask-evopoulos P, Serpetsidaki A, Kaviris G, Kapetanidis V, Papadimitriou P, Voulgaris N, Kassaras I, Vallianatos F et al (2021) Seismic

- waveform data from Greece and Cyprus: Integration, archival and open access, Seismol Res Lett SRL-S-20-00509, submitted
- Evans R (1984) Effects of the free surface on shear wavetrains. *Geophys J Int* 76:165–172. <https://doi.org/10.1111/j.1365-246X.1984.tb05032.x>
- Floyd MA, Billiris H, Paradissis D, Veis G, Avallone A, Briole P, McClusky S, Nocquet JM, Palamartchouk K, Parsons B, England PC (2010) A new velocity field for Greece: Implications for the kinematics and dynamics of the Aegean. *J Geophys Res Solid Earth* 115:1–25. <https://doi.org/10.1029/2009JB007040>
- Ganas A, Elias P, Briole P, Tsironi V, Valkaniotis S, Escartin J, Karasante I, Efstathiou E. (2020) Fault responsible for Samos earthquake identified. *Temblo* <https://doi.org/10.32858/temblor.134>
- Ganas A, Elias P, Kapetanidis V, Valkaniotis S, Briole P, Kassaras I, Argyrakakis P, Barberopoulou A, Moshou A (2019) The July 20, 2017 M6.6 Kos Earthquake: Seismic and Geodetic Evidence for an Active North-Dipping Normal Fault at the Western End of the Gulf of Gökova (SE Aegean Sea). *Pure Appl Geophys* 176:4177–4211. <https://doi.org/10.1007/s00024-019-02154-y>
- Ganas A, Oikonomou AI, Tsimi C (2013) NOFAULTS : a digital database for active faults in Greece. *Bull Geol Soc Greece* 47:518–530
- Gao Y, Crampin S (2004) Observations of stress relaxation before earthquakes. *Geophys J Int* 157:578–582. <https://doi.org/10.1111/j.1365-246X.2004.02207.x>
- Gao Y, Crampin S (2006) A stress-forecast earthquake (with hindsight), where migration of source earthquakes causes anomalies in shear-wave polarisations. *Tectonophysics* 426:253–262. <https://doi.org/10.1016/j.tecto.2006.07.013>
- Gao Y, Crampin S (2008) Shear-wave splitting and earthquake forecasting. *Terra* 20:440–448
- Gao Y, Chen A, Shi Y, Zhang Z, Liu L (2019) Preliminary analysis of crustal shear-wave splitting in the Sanjiang lateral collision zone of the southeast margin of the Tibetan Plateau and its tectonic implications. *Geophys Prospect* 67:2432–2449. <https://doi.org/10.1111/1365-2478.12870>
- Gao Y, Wang P, Zheng S, Wang M, Chen Y, Zhou H (1998) Temporal changes in shear-wave splitting at an isolated swarm of small earthquakes in 1992 near Dongfang, Hainan Island, southern China. *Geophys J Int* 135:102–112. <https://doi.org/10.1046/j.1365-246X.1998.00606.x>
- Gao Y, Wu J, Fukao Y, Shi Y, Zhu A (2011) Shear wave splitting in the crust in North China: Stress, faults and tectonic implications. *Geophys J Int* 187:642–654. <https://doi.org/10.1111/j.1365-246X.2011.05200.x>
- Giannopoulos D, Sokos E, Konstantinou KI, Tselentis GA (2015) Shear wave splitting and V_p/V_s variations before and after the Efpalio earthquake sequence, western Gulf of Corinth, Greece. *Geophys J Int* 200:1436–1448. <https://doi.org/10.1093/gji/ggu467>
- Graham KM, Savage MK, Arnold R, Zal HJ, Okada T, Iio Y, Matsumoto S (2020) Spatio-temporal Analysis of Seismic Anisotropy Associated with the Cook Strait and Kaikōura Earthquake Sequences in New Zealand. *Geophys J Int* 223:1987–2008. <https://doi.org/10.1093/gji/ggaa433>
- Hiramatsu Y, Iwatsuki K, Ueyama S, Iidaka T (2010) Spatial variation in shear wave splitting of the upper crust in the zone of inland high strain rate, central Japan. *Earth, Planets Sp* 62:675–684. <https://doi.org/10.5047/eps.2010.08.003>
- Hunter JD (2007) Matplotlib: A 2D Graphics Environment. *Comput Sci Eng* 9:90–95. <https://doi.org/10.1109/MCSE.2007.55>
- Illsley-Kemp F, Savage MK, Keir D, Hirschberg HP, Bull JM, Gernon TM, Hammond JOS, Kendall JM, Ayele A, Goitom B (2017) Extension and stress during continental breakup: Seismic anisotropy of the crust in Northern Afar. *Earth Planet Sci Lett* 477:41–51. <https://doi.org/10.1016/j.epsl.2017.08.014>
- Ismail WB, Mainprice D (1998) An olivine fabric database: An overview of upper mantle fabrics and seismic anisotropy. *Tectonophysics* 296:145–157. [https://doi.org/10.1016/S0040-1951\(98\)00141-3](https://doi.org/10.1016/S0040-1951(98)00141-3)
- Johnson JH, Savage MK, Townend J (2011) Distinguishing between stress-induced and structural anisotropy at Mount Ruapehu volcano, New Zealand. *J Geophys Res Solid Earth* 116:1–18. <https://doi.org/10.1029/2011JB008308>
- Johnson JH, Savage MK (2012) Tracking volcanic and geothermal activity in the Tongariro Volcanic Centre, New Zealand, with shear wave splitting tomography. *J Volcanol Geotherm Res* 223–224:1–10. <https://doi.org/10.1016/j.jvolgeores.2012.01.017>
- Kapetanidis V, Kassaras I (2019) Contemporary crustal stress of the Greek region deduced from earthquake focal mechanisms. *J Geodyn* 123:55–82. <https://doi.org/10.1016/j.jog.2018.11.004>
- Kassaras I, Kapetanidis V, Ganas A, Tzanis A, Kosma C, Karakonstantis A, Valkaniotis S, Chailas S, Kouskouna V, Papadimitriou P (2020) The New Seismotectonic Atlas of Greece (v1.0) and its Implementation. *Geosciences* 10:447
- Kaviris G, Fountoulakis I, Spingos I, Millas C, Papadimitriou P (2018a) Mantle dynamics beneath Greece from SKS and PKS seismic anisotropy study. *Acta Geophys* 66:1341–1357. <https://doi.org/10.1007/s11600-018-0225-z>
- Kaviris G, Millas C, Spingos I, Kapetanidis V, Fountoulakis I, Papadimitriou P, Voulgaris N, Makropoulos K (2018b) Observations of shear-wave splitting parameters in the Western Gulf of Corinth focusing on the 2014 $M_w=5.0$ earthquake. *Phys Earth Planet Inter* 282:60–76. <https://doi.org/10.1016/j.pepi.2018.07.005>
- Kaviris G, Spingos I, Kapetanidis V, Papadimitriou P, Voulgaris N, Makropoulos K (2017) Upper crust seismic anisotropy study and temporal variations of shear-wave splitting parameters in the Western Gulf of Corinth (Greece) during 2013. *Phys Earth Planet Inter* 269:148–164
- Kaviris G, Spingos I, Millas C, Kapetanidis V, Fountoulakis I, Papadimitriou P, Voulgaris N, Drakatos G (2018c) Effects of the January 2018 seismic sequence on shear-wave splitting in the upper crust of Marathon (NE Attica, Greece). *Phys Earth Planet Inter* 285:45–58. <https://doi.org/10.1016/j.pepi.2018.10.007>
- Kaviris G, Spingos I, Karakostas V, Papadimitriou E, Tsapanos T (2020) Shear-wave splitting properties of the upper crust, during the 2013–2014 seismic crisis, in the CO₂-rich field of Florina Basin. Greece *Phys Earth Planet Inter* 106503. <https://doi.org/10.1016/j.pepi.2020.106503>
- Kiratzis A (2018) The 12 June 2017 M_w 6.3 Lesbos Island (Aegean Sea) earthquake: Slip model and directivity estimated with finite-fault inversion. *Tectonophysics* 724–725:1–10. <https://doi.org/10.1016/j.tecto.2018.01.003>
- Kouskouna V, Sakkas G (2013) The University of Athens Hellenic Macroseismic Database (HMDB.UoA): historical earthquakes. *J Seis* 17:1253–1280. <https://doi.org/10.1007/s10950-013-9390-3>
- Kreemer C (2009) Absolute plate motions constrained by shear wave splitting orientations with implications for hot spot motions and mantle flow. *J Geophys Res Solid Earth* 114:1–18. <https://doi.org/10.1029/2009JB006416>
- Kreemer C, Chamot-Rooke N (2004) Contemporary kinematics of the southern Aegean and the Mediterranean Ridge. *Geophys J Int* 157:1377–1392. <https://doi.org/10.1111/j.1365-246X.2004.02270.x>
- Krischer L, Megies T, Barsch R, Beyreuther M, Lecocq T, Caudron C, Wassermann J (2015) ObsPy: A bridge for seismology into the scientific Python ecosystem. *Comput Sci Discov* 8:17. <https://doi.org/10.1088/1749-4699/8/1/014003>
- Liu S, Crampin S, Luckett R, Yang J (2010) A deterministic short-term precursor to the 2010 Eyjafjallajökull eruption in Iceland. *Geogr J* 177:4–11. <https://doi.org/10.1111/j.1475-4959.2010.00379.x>
- Makropoulos K, Kaviris G, Kouskouna V (2012) An updated and extended earthquake catalogue for Greece and adjacent areas since

1900. *Nat Hazards Earth Syst Sci* 12:1425–1430. <https://doi.org/10.5194/nhess-12-1425-2012>
- Margheriti L, Ferulano MF, Di Bona M (2006) Seismic anisotropy and its relation with crust structure and stress field in the Reggio Emilia Region (Northern Italy). *Geophys J Int* 167:1035–1043. <https://doi.org/10.1111/j.1365-246X.2006.03168.x>
- McClusky S, Balassanian S, Barka A, Demir C, Ergintav S, Georgiev I, Gurkan O, Hamburger M, Hurst K, Kahle H et al (2000) Global Positioning System constraints on plate kinematics and dynamics in the eastern Mediterranean and Caucasus. *J Geophys Res Solid Earth* 105:5695–5719. <https://doi.org/10.1029/1999jb900351>
- Montagner JP, Tanimoto T (1991) Global upper mantle tomography of seismic velocities and anisotropies. *J Geophys Res* 96:20337. <https://doi.org/10.1029/91JB01890>
- Nolte KA, Tsoflias GP, Bidgoli TS, Watney WL (2017) Shear-wave anisotropy reveals pore fluid pressure-induced seismicity in the U.S. midcontinent. *Sci Adv* 3:1700443
- Ocakoglu N, Demirbağ E, Kuşçu I (2005) Neotectonic structures in İzmir Gulf and surrounding regions (western Turkey): Evidences of strike-slip faulting with compression in the Aegean extensional regime. *Mar Geol* 219:155–171. <https://doi.org/10.1016/j.margeo.2005.06.004>
- Papadimitriou EE, Sykes LR (2001) Evolution of the stress field in the Northern Aegean Sea (Greece). *Geophys J Int* 146:747–759. <https://doi.org/10.1046/j.0956-540X.2001.01486.x>
- Papadimitriou P, Kapetanidis V, Karakonstantis A, Spingos I, Kassaras I, Sakkas V, Kouskouna V, Karatzetou A, Pavlou K, Kaviris G, Voulgaris N (2020) First Results on the $M_w=6.9$ Samos Earthquake of 30 October 2020. *Bull Geol Soc Greece* <https://doi.org/10.12681/bgsg.25359>
- Papadimitriou P, Kassaras I, Kaviris G, Tselentis GA, Voulgaris N, Lekkas E, Chouliaras G, Evangelidis C, Pavlou K, Kapetanidis V et al (2018) The 12th June 2017 $M_w=6.3$ Lesbos earthquake from detailed seismological observations. *J Geodyn* 115:23–42. <https://doi.org/10.1016/j.jog.2018.01.009>
- Papadimitriou P, Kaviris G, Makropoulos K (1999) Evidence of shear-wave splitting in the eastern Corinthian Gulf (Greece). *Phys Earth Planet Inter* 114:3–13. [https://doi.org/10.1016/S0031-9201\(99\)00041-2](https://doi.org/10.1016/S0031-9201(99)00041-2)
- Pastori M, Baccheschi P, Margheriti L (2019) Shear Wave Splitting Evidence and Relations With Stress Field and Major Faults From the “Amatrice-Visso-Norcia Seismic Sequence.” *Tectonics* 38:3351–3372. <https://doi.org/10.1029/2018TC005478>
- Paulssen H (2004) Crustal anisotropy in southern California from local earthquake data. *Geophys Res Lett* 31:1601. <https://doi.org/10.1029/2003GL018654>
- Peng Z, Ben-Zion Y (2004) Systematic analysis of crustal anisotropy along the Karadere-Düzce branch of the North Anatolian fault. *Geophys J Int* 159:253–274. <https://doi.org/10.1111/j.1365-246X.2004.02379.x>
- Piccinini D, Margheriti L, Chiaraluce L, Cocco M (2006) Space and time variations of crustal anisotropy during the 1997 Umbria-Marche, central Italy, seismic sequence. *Geophys J Int* 167:1482–1490. <https://doi.org/10.1111/j.1365-246X.2006.03112.x>
- Ring U, Will T, Glodny J, Kumerics C, Gessner K, Thomson S, Güngör T, Monié P, Okrusch M, Drüppel K (2007) Early exhumation of high-pressure rocks in extrusion wedges: Cycladic blueschist unit in the eastern Aegean, Greece, and Turkey. *Tectonics* 26:TC2001 <https://doi.org/10.1029/2005TC001872>
- Salimbeni S, Pondrelli S, Margheriti L, Park J, Levin V (2008) SKS splitting measurements beneath Northern Apennines region: A case of oblique trench-retreat. *Tectonophysics* 462:68–82. <https://doi.org/10.1016/j.tecto.2007.11.075>
- Savage MK, Wessel A, Teanby NA, Hurst AW (2010) Automatic measurement of shear wave splitting and applications to time varying anisotropy at Mount Ruapehu volcano, New Zealand. *J Geophys Res Solid Earth*. <https://doi.org/10.1029/2010JB007722>
- Shi Y, Gao Y, Shen X, Liu KH (2020) Multiscale spatial distribution of crustal seismic anisotropy beneath the northeastern margin of the Tibetan plateau and tectonic implications of the Haiyuan fault. *Tectonophysics* 774:228274. <https://doi.org/10.1016/j.tecto.2019.228274>
- Silver PG, Chan WW (1991) Shear wave splitting and subcontinental mantle deformation. *J Geophys Res Solid* 96:16429–16454. <https://doi.org/10.1029/91JB00899>
- Spingos I, Kaviris G, Millas G, Papadimitriou P, Voulgaris N (2020) Pytheas: An open-source software solution for local shear-wave splitting studies. *Comput Geosci* 134:104346. <https://doi.org/10.1016/j.cageo.2019.104346>
- Stamatakis M, Tziritis E, Evelpidou N (2009) The geochemistry of Boron-rich groundwater of the Karlovassi Basin, Samos Island, Greece. *Cent Eur J Geosci* 1:207–218. <https://doi.org/10.2478/v10085-009-0017-4>
- Stucchi M, Rovida A, Gomez Capera AA, Alexandre P, Camelbeeck T, Demircioglu MB, Gasperini P, Kouskouna V, Musson RMW, Radulian M, Sesetyan K, Vilanova S, Baumont D, Bungum H et al (2013) The SHARE European Earthquake Catalogue (SHEEC) 1000–1899. *J Seismol* 17:523–544. <https://doi.org/10.1007/s10950-012-9335-2>
- Tan O, Papadimitriou EE, Pabuccu Z, Karakostas V, Yörük A, Lep-tokaropoulos K (2014) A detailed analysis of microseismicity in Samos and Kusadasi (Eastern Aegean Sea) areas. *Acta Geophys* 62:1283–1309. <https://doi.org/10.2478/s11600-013-0194-1>
- Teanby NA, Kendall JM, van der Baan M (2004) Automation of shear-wave splitting measurements using cluster analysis. *Bulliten Seismol Soc Am* 94:453–463. <https://doi.org/10.1785/0120030123>
- Triantafyllou I, Gogou M, Mavroulis S, Lekkas E, Papadopoulos GA, Thravolos M (2021) The Tsunami Caused by the 30 October 2020 Samos (Aegean Sea) $M_w7.0$ Earthquake: Hydrodynamic Features, Source Properties and Impact Assessment from Post-Event Field Survey and Video Records. *J. Marine Sci Engin* 9(1):68
- Unglert K, Savage MK, Fournier N, Ohkura T, Abe Y (2011) Shear wave splitting, vP/vS, and GPS during a time of enhanced activity at Aso caldera Kyushu. *J Geophys Res Solid Earth*. <https://doi.org/10.1029/2011JB008520>
- Valcke SLA, Casey M, Lloyd GE, Kendall JM, Fisher QJ (2006) Lattice preferred orientation and seismic anisotropy in sedimentary rocks. *Geophys J Int* 166:652–666. <https://doi.org/10.1111/j.1365-246X.2006.02987.x>
- Walsh E, Arnold R, Savage MK (2013) Silver and Chan revisited. *J Geophys Res Solid Earth* 118:5500–5515. <https://doi.org/10.1002/jgrb.50386>
- Wessel P, Luis JF, Uieda L, Scharroo R, Wobbe F, Smith WHF, Tian D (2019) The Generic Mapping Tools Version 6. *Geochem Geophys Geosys* 20:5556–5564. <https://doi.org/10.1029/2019GC008515>
- Wüstefeld A, Bokelmann G (2007) Null detection in shear-wave splitting measurements. *Bull Seismol Soc Am* 97:1204–1211. <https://doi.org/10.1785/0120060190>
- Yolsal-Çevikbilen S, Taymaz T, Helvacı C (2014) Earthquake mechanisms in the Gulfs of Gökova, Siğacık, Kuşadasi, and the Simav Region (western Turkey): Neotectonics, seismotectonics and geodynamic implications. *Tectonophysics* 635:100–124. <https://doi.org/10.1016/j.tecto.2014.05.001>
- Zatsepin S, Crampin S (1997) Modelling the compliance of crustal rock—I. Response of shear-wave splitting to differential stress. *Geophys J Int* 129:477–494. <https://doi.org/10.1111/j.1365-246X.1997.tb04488.x>
- Zinke JC, Zoback MD (2000) Structure-related and stress-induced shear-wave velocity anisotropy: Observations from microearthquakes near the Calaveras Fault in Central California. *Bull Seismol Soc Am* 90:1305–1312. <https://doi.org/10.1785/0119990099>